Hindawi
Scientific Programming
Volume 2021, Article ID 2430380, 11 pages
https://doi.org/10.1155/2021/2430380

Research Article

Denoising of Degenerative Lumbar Spine Lesions MRI Images Using Block-Matching and 3D Filtering

Yongzhao Zhang, Jianshi Yin, Han Yan, Jun Liu, and Junsheng Wang

Department of Orthopedics, The 967th Hospital of Joint Logistics Support Force of Chinese People's Liberation Army, Dalian 116021, China

Correspondence should be addressed to Junsheng Wang; 201711004121@stu.zjsru.edu.cn

Received 22 September 2021; Revised 9 November 2021; Accepted 11 November 2021; Published 9 December 2021

Academic Editor: M. Pallikonda Rajasekaran

This work was aimed to explore the application of the L_2-block-matching and 3-dimentional filtering (BM3D) (L_2-BM3D) denoising algorithm in the treatment of lumbar degeneration with long- and short-segment fixation of posterior decompression. 120 patients with degenerative lumbar scoliosis were randomly divided into group A (MRI images were not processed), group B (MRI images were processed by the BM3D denoising algorithm), and group C (MRI images were processed by the BM3D denoising algorithm based on weighted norm L_2). This denoising algorithm was comprehensively evaluated in terms of mean square error (MSE), peak signal-to-noise ratio (PSNR), structural similarity index measure (SSIM), and running time. Besides, the results of surgeries based on different denoising methods were assessed through the surgical time, intraoperative blood loss, postoperative drainage, and postoperative follow-up. The results showed the following: (1) PSNR (peak signal-to-noise ratio) and SSIM (structural similarity index measure) of the L_2-BM3D algorithm are better than those of the BM3D algorithm (31.21 dB versus 29.33 dB, 0.83 versus 0.72), while mean square error (MSE) was less than that of the BM3D algorithm ($P < 0.05$). (2) The operation time, intraoperative bleeding, and postoperative drainage volume in group C were lower than those in group B and group A ($P < 0.05$). The postoperative follow-up results showed that, in group C, the postoperative VAS (visual analysis scale) score (1.03 ± 0.29) and ODI (Oswestry disability index) (9.29 ± 0.32) were lower, indicating that the postoperative recovery effect of patients was better. Therefore, the patient's postoperative recovery effect was better. In conclusion, the L_2-BM3D algorithm had an ideal denoising effect on MRI images of lumbar degeneration and was worthy of clinical promotion.

1. Introduction

Studies suggested that degenerative lumbar lesions were one of the main causes of low back pain. With the aging of our society, the incidence rate of degenerative lumbar diseases was increasing [1, 2]. Lumbar degeneration can cause lumbar scoliosis, spinal canal stenosis, and degenerative spondylolisthesis. The main clinical manifestations were low back pain, lower limb weakness, pacing, nerve root pain, paralysis, and so on [3]. Although most patients can get better by treatment, the treatment of lumbar degeneration is still a problem that needs attention for elderly patients with severe symptoms [4], especially spinal displacement [5]. At present, surgery is the main method for the treatment of degenerative lumbar scoliosis, including osteotomy, posterior decompression, and internal fixation [6]. According to the length of fixed segments, internal fixation can be divided into long-segment fixation (fusion fixation segments >5 or average >5) and short-segment fixation (fusion fixation segments <5 or average <5). Long-segment surgery is mostly used in patients with severe scoliosis, which is difficult and prone to complications. Short-segment surgery is mostly used for patients with mild scoliosis, with less postoperative trauma and less impact on postoperative activities [7, 8]. Due to the most occurrence in the elderly and physical reasons, a variety of surgical contraindications may exist, clinical surgical treatment is difficult, and there are many postoperative complications [9]. Therefore, the choice of surgical methods is very critical.

At present, the clinical examination methods for degenerative lumbar scoliosis include X-ray, computed tomography (CT), radionuclide imaging, and MRI [10].

X-ray includes ordinary X-ray examination and X-ray radiography. Ordinary X-ray examination has simple operation and good economy, but the examination effect is poor. X-ray radiography is a dynamic examination method with good examination effect [11], but it is an invasive examination. Due to the need to inject contrast medium into patients, there is a certain risk of infection and complications. Thus, the acceptance of doctors and patients is low [12]. Although CT examination has short time, high image resolution, and no obvious contraindications, the degree of diagnosis of the disease is not high and lacks clear diagnostic significance [13]. Radionuclide imaging is mostly used in tumor related diseases, and its application in lumbar degeneration needs to be studied.

MRI has high resolution for soft tissues, and the sagittal image is a single-shot imaging. Its multidirectional imaging characteristics fully and accurately reflect the position and state of the lumbar spine. However, MRI will inevitably introduce some machine noises in the process of data acquisition because of its own limitations, resulting in blurred anatomical information on the image, poor image quality, and interference with clinicians' visual detection, making it very difficult for subsequent lesion analysis [14, 15]. Therefore, how to get out the noises of medical images and keep more detailed information as much as possible is very necessary for subsequent clinical treatment.

With the development of intelligent denoising algorithm, it has been proposed that block-matching and 3D filtering (BM3D) algorithm [16] is the most advanced denoising technology at present, which can achieve better denoising compared with any other existing methods. A large number of studies have proposed that BM3D algorithm has also obtained good research results in the processing of medical image images [17, 18]. Xu et al. [19] have used it for DWI image denoising. As a result, the method has achieved good denoising effect without causing fringe artifacts. However, BM3D algorithm still has room for improvement to achieve high-quality denoising. The weighted L_2 norm can constrain the spatial difference image cube, effectively explore the shared group sparse mode, and achieve good results in the calculation of the algorithm [20].

In summary, in this study, the BM3D denoising algorithm will be used based on weighted L_2 norm to process MRI images and for disease diagnosis of degenerative lumbar scoliosis patients. The application value of the algorithm will be evaluated by observing the treatment effect of this method in the diagnosis of degenerative lumbar scoliosis patients, so as to provide more research basis for clinical patients to obtain more effective diagnosis and treatment methods.

2. Materials and Methods

2.1. Research Objects. In this study, 120 patients with degenerative lumbar scoliosis who were treated at hospital from June 2017 to June 2019 were selected as the research objects. Besides, each patient underwent MRI examination. According to different denoising methods, 120 patients were rolled into 3 groups (group A, group B, and group C). In group A, there were 20 males and 20 females, aged 27–66 years, with an average age of 52 ± 13.3 years. The MRI images of the patients from group A were not denoised. 15 males and 25 females were included in group B, aged 29–65 years, with an average age of 52 ± 12.1 years. What is more, their MRI images were denoised by the BM3D denoising algorithm. There were 19 males and 21 females in group C, aged 26–69 years, with an average age of 53 ± 13.1 years. The BM3D denoising algorithm based on the weighted norm L_2 was employed to denoise the MRI images of patients from group C. After the denoising, the short- and long-segment fixation treatments of posterior decompression were specifically adopted in all patients according to the different degree of degeneration. This experiment had been authorized by the Medical Ethics Committee of the hospital, and the patients and their family members had been aware of this experiment and had signed the informed consent forms.

The criteria for inclusion were defined as follows: patients who were older than 20 years of age and younger than 70 years of age and were diagnosed with degenerative lumbar disease, had normal organs or systems, and had complete clinical data.

The criteria for exclusion were defined as follows: patients who had undergone surgical treatment, could not receive the MRI scanning or had refused to undergo MRI scanning, suffered from other organ or system diseases, had incomplete clinical data, and were not suitable for this experiment for other reasons.

2.2. Image Denoising Method Based on BM3D Algorithm. The BM3D algorithm is a denoising method based on image blocks. The specific operation was to divide the images with noises into many image domains, each image was denoised separately, and the denoised image domains were reaggregated, so as to form the final image with higher signal-to-noise ratio (SNR) [21]. Figure 1 illustrates the specific process.

In the actual operation of the BM3D algorithm, P was considered as the input noise image, so the following equation could be obtained:

$$P(x) = P'(x) + n(x), \quad x \in I. \tag{1}$$

In equation (1), P represents the original image, P' means the real noise-free image, n stands for the Gaussian white noise with the mean value of 0 and the variance of σ^2, and x expresses a pixel on the image. Image P was for matching processing, and similar blocks were searched in image P. When P' was available, the similarity between blocks could be calculated by the following equation:

$$d'(C, C_x) = \frac{\left\| Z - Z_x \right\|_2^2}{N'^2}. \tag{2}$$

In equation (2), C represents the reference block, C_x expresses a matching block with the size of $N \times N$ at point x

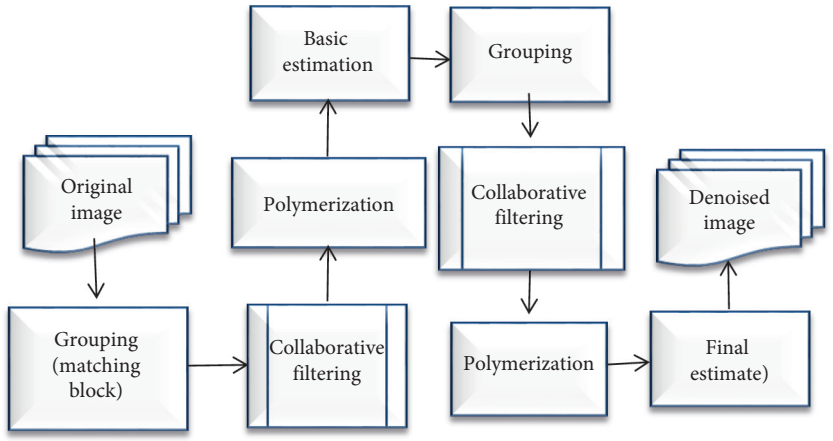

Figure 1: Flow chart of BM3D algorithm denoising.

in image P, Z and Z_x stand for the reference block and the image block in turn, respectively, when the real image P was only available, d' represents the similarity between the blocks, N' means the size of the image block during basic estimation, and $_2$ expresses the norm of L_2. When only the original image P was available, the similarity between blocks could be calculated by the following equation:

$$d(C, C_x) = \frac{\|C - C_x\|_2^2}{N'^2}. \tag{3}$$

Assuming that C and C_x did not overlap, the expectation could be expressed as a noncentral chi-square random distribution, which is shown in the following equation:

$$E\{d(C, C_x)\} = d'(C, C_x) + 2\sigma^2. \tag{4}$$

When searching, the noise in the original image would affect the matching results [22]. A prefilter was added to avoid this problem when calculating the similarity between blocks. Besides, it could be expressed as follows:

$$d(C, C_x) = \frac{\|\gamma'[T'_{2D}(C)] - \gamma'[T'_{2D}(C_x)]\|_2^2}{N''^2}. \tag{5}$$

In equation (5), $\gamma\prime$ represents the hard threshold filter factor and T'_{2D} stands for the linear transformation of the 2-dimensional image, and equation (5) was adopted to obtain the block-matching result, as shown in the following:

$$N'_{\max} = \{x \in I: d(C, C_x) \le \tau'_{\text{match}} \tag{6}$$

In equation (6), $N'_{\max}$ represents the number of all similar blocks, and τ'_{match} stands for the maximum distance between two image blocks that were similar. $C_{N'_{\max}}$ was employed to represent the set composed by all $N'_{\max}$, and the collaborative filtering of $C_{N'_{\max}}$ needed to be realized by the hard-valued filtering in the 3-dimensional transformation. Then, the 3-dimensional group estimation value could be obtained as follows through the 3-dimensional hard-valued filter to reduce the noise and inverse transformation:

$$\widehat{G}_{N'_{\max}} = T'^{-1}_{3D}\left(\gamma\left(T'_{3D}\left(C_{N'_{\max}}\right)\right)\right). \tag{7}$$

In equation (7), $\widehat{G}_{N'_{\max}}$, T'_{3D}, and T'^{-1}_{3D} stand for the basic estimated value of each reference block, the linear transformation of the 3-dimensional image, and the inverse transformation of the 3-dimensional linear transformation, respectively. The basic estimation image could be gotten by gathering all reference blocks, which can be expressed as follows:

$$\widehat{g}^{\text{basic}}(x) = \frac{\sum_{x \in I} \sum_{x_m \in N'_{\max}} \omega\prime \widehat{G}^{'x}_{x_m}(x)}{\sum_{x \in I} \sum_{x_m \in N'_{\max}} \omega\prime \chi_{x_m}(x)}, \quad \forall x \in X. \tag{8}$$

In equation (8), ω' expresses the weight during aggregation, and χ_{x_m} means the feature function of similar blocks. After the basic estimation was completed, the noise was largely removed. Then, the basic estimation was used as the input of the second step, and the 3-dimensional matrix was processed in cooperation with Wiener filtering to obtain the final filtered image. $N''_{\max}$ represents the set of image block coordinates in the final estimation, so it could be expressed as follows:

$$N''_{\max} = \left\{ x \in I: \left\| \frac{\widehat{G}^{\text{basic}} - \widehat{G}^{\text{basic}}_x \|_2^2}{(N'')^2} < \tau''_{\text{match}} \right. . \tag{9}$$

In equation (9), τ''_{match} stands for the maximum distance between two similar blocks in the final estimation stage. The image obtained by the basic estimation was taken as a reference, so as to obtain the shrinkage coefficient of the Wiener filter, as shown in the following equation:

$$W_{N''_{\max}} = \left| T''_{3D}\left(\frac{\widehat{G}^{\text{basic}}_{N''_{\max}})|^2}{\left| T''_{3D}\left(\widehat{G}^{\text{basic}}_{N''_{\max}}\right)\right| + \sigma^2}. \right. \right. \tag{10}$$

The inverse transformation of the 3-dimensional linear transformation was applied to obtain the estimated value of the similar block at $x \in N''_{\max}$, which could be calculated as follows:

$$\widehat{G}''_{N''_{\max}} = T''^{-1}_{3d}\left[W_{N''_{\max}} T''_{3d}\left(C_{N''_{\max}}\right)\right]. \tag{11}$$

In equations (10) and (11), $\widehat{G}^{basic}_{N'_{\max}}$, $C_{N''_{\max}}$, T''_{3D}, and $T^{-1''}_{3D}$ represent the basic estimation image, the set composed of all $N''_{\max}$ in the final estimation stage, the linear transformation of the 3-dimensional image, and the inverse transformation of the 3-dimensional transformation, respectively. According to the weight of each pixel x, the basic images of all reference blocks were gathered to get the final estimate of the image, as shown in the following equation:

$$\widehat{g}^{\text{final}}(x) = \frac{\sum_{x\in I}\sum_{x_m\in N'_{\max}}\omega''\widehat{G}^{''x}_{x_m}(x)}{\sum_{x\in I}\sum_{x_m\in N'_{\max}}\omega''\chi_{x_m}(x)}, \quad \forall x \in X. \tag{12}$$

The BM3D denoising algorithm had a good denoising effect, but its search time was long, and the calculation time and complexity were high. When the noise was too high, the similarity between the reference block and the similar block could not be guaranteed, but the denoising effect was greatly reduced [16, 23]. In order to improve the insufficient similar block measurement in the traditional BM3D denoising algorithm, an image block similarity calculation method was proposed in this study based on weighted norm L_2.

The norm L_2 of the traditional BM3D denoising algorithm did not take into account the internal structure of the image when calculating the similarity between image blocks, but the gray-scale difference of the corresponding similar points of the image block was only considered [24]. Thus, the interblock distance of the weighted norm L_2 was defined as follows:

$$d(M,N) = n^{-2}\sum_{i=1}^{n}\sum_{l=1}^{n} d_{il}(M,N). \tag{13}$$

In equation (13), $d_{il}(M,N)$ stands for the distance between the $3*3$ windows centered on pixels M_{il} and N_{il}, and its calculation method could be expressed by the following equation:

$$d_{il}(H,G) = \sum\left(W^H_{il}\circ\left(\text{Win}\left(h_{il}\right) - \text{Win}\left(g_{il}\right)\right)^2\circ W^G_{il}\right). \tag{14}$$

In equation (14), W^H_{il} and W^G_{il} represent the weight matrixes, which were the contributions of pixels around h_{il} and g_{il} to them, and $\circ$ stands for the multiplication of the elements at the corresponding positions of the matrix. Then, the similarity of pixels on the image was calculated according to their respective normalization factors degree, as shown in the following equation:

$$w^H = \exp\left(\frac{\left\|h_{p,q} - h_{i,l}\right\|^2_2}{h^2}\right). \tag{15}$$

The algorithm contributed the most only by ensuring the maximum value of w^G and w^H, and the improved norm L_2 calculation method not only took into account the similarity between image blocks but also considered the similarity of pixels within the image block, thereby promoting the matching accuracy and preserving the image details as much as possible.

2.3. MRI Examination. First, the patients were instructed to relax before scanning. During scanning, the patient shall be scanned to determine the location of the disease. After coronal scanning, the scanning sequence included T1-weighted imaging (T1WI), T2-weighted imaging (T2WI), and dynamic contrast enhanced magnetic resonance imaging (DCE-MRI). Table 1 presents the specific scanning sequence parameters.

2.4. Surgical Methods. MRI images of patients were denoised by different algorithms, and posterior decompression pedicle screw fixation and fusion were performed according to the degree of lumbar scoliosis. During the surgery, the patient was under general anesthesia and was in a prone position. The posterior approach was chosen, and the facet joint process and upper and lower vertebrae of patient were exposed after the posterior median incision. After a screw was placed in the patient's vertebral body, some of the lamina and spinous process was bitten off, the corresponding intervertebral space was stretched, and the bitten part of the lamina and spinous process was properly trimmed to remove the hyperplasia and stubbornness around the lesion to achieve decompression. According to the degree of scoliosis of the patient, the pedicle connecting rod with the appropriate length was chosen and prebent to the appropriate curvature, which was set in both sides of the diseased vertebral body. Then, the appropriate pressure was put to the convex square, so as to correct the scoliosis. Finally, the position of the sagittal plane was adjusted appropriately and the top cap was tightened. After the surgery was completed, the incision was cleaned with sterile normal saline and the drainage tube was indwelled, so the incision was sutured. The infection prevention medication was used for 4–8 days after the surgery. In addition, the postoperative care and regular follow-up work should be done well.

2.5. Evaluation Indexes. With the help of MSE (mean square error), PSNR (peak signal-to-noise ratio), SSIM (structural similarity index measure), and running time, the denoising effects of different denoising algorithms were analyzed by comprehensive evaluation.

MSE was employed to evaluate the image quality by calculating the mean square values between different denoising algorithms. The smaller the MSE value, the better the denoising effect of the algorithm. The calculation of MSE is shown in the following equation:

$$\text{MSE} = \frac{\sum_{i=1}^{A}\sum_{j=1}^{B}\left[x(i.j) - y(i,j)\right]^2}{AB}. \tag{16}$$

In the above equation, A represents the height of the image, B represents the width of the image, and AB represents the size of the image.

PSNR represents the SNR of the image after noise removal. The larger the PSNR value, the better the image quality. What is more, PSNR could be calculated as follows:

Table 1: MRI scanning parameters.

Scan sequence	T1WI	T2WI	DCE-MRI
TE (ms)	8.5	87	2
TR (ms)	189	3221	3
FOV (mm)	122 × 122	61 × 61	102 × 102
Layer thickness (mm)	2.4	2.4	2.4
Spacing (mm)	1	1	1
Matrix	256 × 256	120 × 120	130 × 130
Number of layers	9	9	9

$$\mathrm{PSNR}(x, y) = 10 \times \log_{10}\left(\frac{\max\left[y^2(i, j)\right]}{\mathrm{MSE}}\right). \tag{17}$$

SSIM was adopted to assess the similarity of denoised images from three aspects (structure, brightness, and contrast). The larger the SSIM, the better the quality of the denoised images. Besides, α, β, and γ stand for the weighting factors, and the SSIM could be expressed as follows:

$$\mathrm{SSIM}(x, y) = s(x, y)^{\alpha} \bullet l(x, y)^{\beta} \bullet c(x, y)^{\gamma}. \tag{18}$$

Observation indexes after surgery included the surgical time, intraoperative blood loss, and postoperative drainage. There was a 12-month follow-up for every patient after the surgery. The VAS was applied to score the postoperative pain of the patients, and its total score was 10 points. The higher the score, the stronger the pain. The ODI was employed to evaluate the patient's daily action function after surgery, and the total score was 40 points. The higher the score was, the more seriously the daily action was affected.

2.6. Statistical Analysis. In this study, SPSS 19.0 software was used for data processing, measurement data were expressed as mean ± standard deviation, and classification data were compared and tested by χ^2. The data comparison between groups was made by SNK-q test, and parameter correlation was analyzed by Pearson. In addition, $P < 0.05$ indicated that the difference was statistically substantial.

3. Experimental Results

3.1. Evaluation of Image Denoising Quality. Figures 2–4 are, respectively, under different noise levels ($\sigma = 10/15/20$), BM3D algorithm, and MRI image processed by the L_2-BM3D algorithm. It was found that the BM3D algorithm had a reliable denoising effect on the images. But the expected denoising effect could not be achieved when the noise intensity was too high. After improving the weighted norm L_2, the images' details were better preserved and the denoising effect was better.

The 3 denoising algorithms were assessed in terms of MSE, PSNR, SSIM, and running time. The results showed that the PSNR values of the BM3D algorithm and the L_2-BM3D algorithm were 29.33 dB and 31.21 dB, respectively (Figure 5), and their SSIM values were 0.72 and 0.83, respectively (Figure 6). Thus, the difference between the two was statistically obvious ($P < 0.05$). However, the running times of the above algorithms were 35.25 s and 36.63 s, respectively (Figure 7), and there was no statistically huge difference between them ($P > 0.05$). The MSE values of the two denoising algorithms were compared, finding that the error vector of the L_2-BM3D denoising algorithm was smaller than the error vector of the BM3D denoising algorithm (Figure 8). Therefore, it was indicated that the L_2-BM3D denoising algorithm had a higher denoising image quality.

3.2. Comparison of Surgical Effects Based on Different Denoising Algorithms. After the surgery, the surgical results were evaluated from three aspects: surgical time, intraoperative blood loss, and postoperative drainage. Due to the different degrees of lumbar degeneration of the patients, different segmental fixation treatments were adopted during the surgery. In group A, there were 25 cases and 15 cases with posterior decompression short-segment fixation and long-segment fixation, respectively. Besides, their average surgical times were 180 ± 9.33 min and 289 ± 6.26 min, respectively (Figure 9), their average intraoperative blood losses were 305 ± 12.15 mL and 569 ± 15.33 mL, respectively (Figure 10), and their average postoperative drainage volumes were 189 ± 9.25 mL and 338 ± 11.91 mL, respectively (Figure 11). In group B, 23 cases had posterior decompression short-segment fixation, with average surgical time, intraoperative blood loss, and postoperative drainage volume of 168 ± 12.65 min, 274 ± 15.66 mL, and 159 ± 6.99 mL, respectively. What is more, there were 17 cases of posterior decompression long-segment fixation, and the average surgical time, intraoperative blood loss, and postoperative drainage volume were 268 ± 9.21 min, 528 ± 14.12 mL, and 301 ± 9.47 mL, respectively. 28 cases and 12 cases from group C underwent the posterior decompression short-segment fixation and long-segment fixation, respectively. The average surgical times were 151 ± 5.45 min (short-segment fixation) and 249 ± 6.41 min (long-segment fixation), the average intraoperative blood losses were 255 ± 9.98 mL (short-segment fixation) and 482 ± 11.31 mL (long-segment fixation), and the average postoperative drainage volumes were 142 ± 6.27 mL (short-segment fixation) and 279 ± 10.81 mL (long-segment fixation). Therefore, the above difference between the groups was statistically substantial ($P < 0.05$).

3.3. Comparison of Postoperative Follow-Up Results Based on Different Denoising Algorithms. After the surgery, the patients were followed up every 3 months, and the last follow-up was at the 12th month after surgery. Then, the VAS and ODI of all patients were evaluated, and their comparison results are shown in Figures 12-13. The results showed that the postoperative VAS and ODI of patients with short-segment surgeries based on the L_2-BM3D denoising method were 1.03 ± 0.29 and 9.29 ± 0.32 at the last follow-up, respectively. Moreover, the postoperative VAS and ODI of patients with long-segment surgeries based on the L_2-BM3D denoising method were 1.21 ± 0.11 and 10.33 ± 1.16, respectively. Therefore, the postoperative VAS and ODI of patients with short-segment surgeries were sharply lower

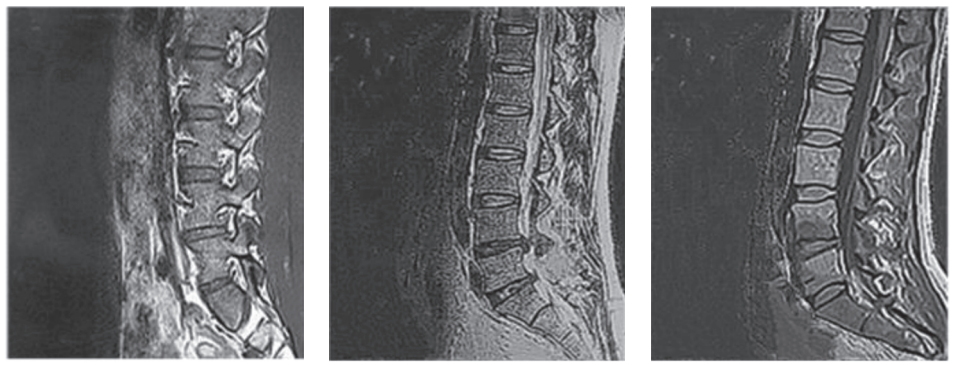

(a) (b) (c)

Figure 2: The MRI images with noises. (a) $\sigma = 10$, (b) $\sigma = 15$, and (c) $\sigma = 20$.

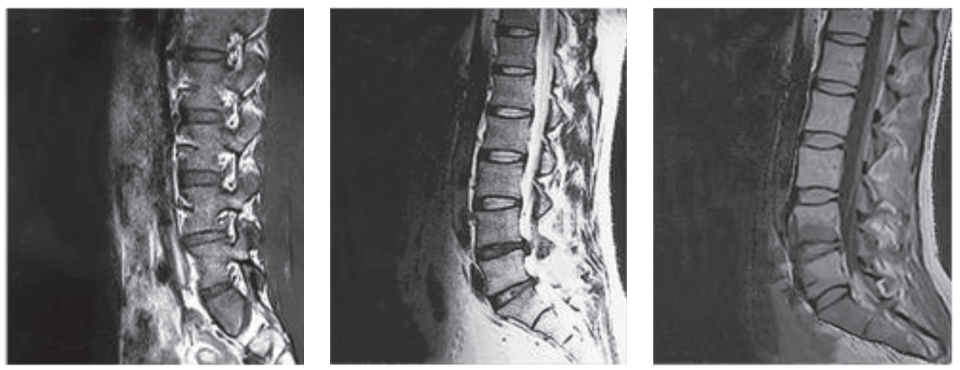

(a) (b) (c)

Figure 3: Denoising effect of the BM3D algorithm. (a) $\sigma = 10$, (b) $\sigma = 15$, and (c) $\sigma = 20$.

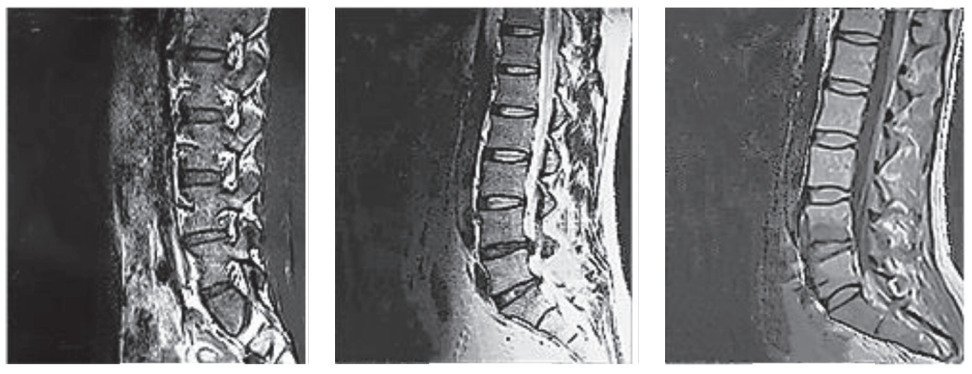

(a) (b) (c)

Figure 4: BM3D image denoising effects based on weighted norm L_2. (a) $\sigma = 10$, (b) $\sigma = 15$, and (c) $\sigma = 20$.

than those of patients with long-segment surgeries based on the L_2-BM3D denoising method ($P < 0.05$).

4. Discussion

In order to investigate the application of different denoising algorithms for processing MRI medical images in the treatment of lumbar degeneration with long- and short-segment fixation after decompression, the BM3D denoising algorithm was improved in this study to propose the image block similarity calculation method L_2-BM3D based on weighted norm L_2. Then, the L_2-BM3D denoising algorithm was adopted to analyze the denoising effect and clinical surgery effect, which were compared with those of the BM3D denoising algorithm. With the help of MSE, PSNR, SSIM, and running time, the denoising algorithm was evaluated to help verify the advantages of the L_2-BM3D denoising algorithm.

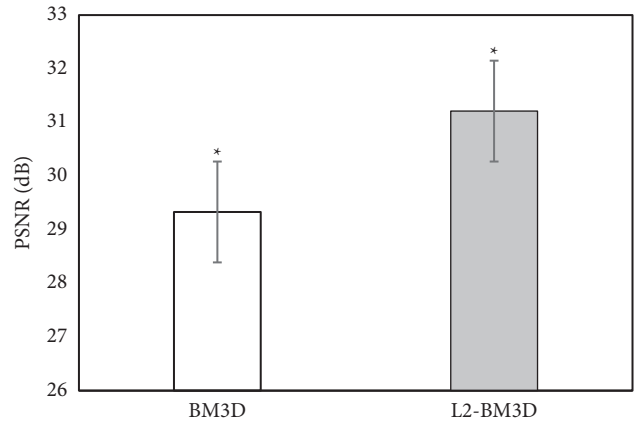

Figure 5: Comparison of PSNR values of different denoising algorithms. Note: "*" indicates that the comparison was statistically significant ($P < 0.05$).

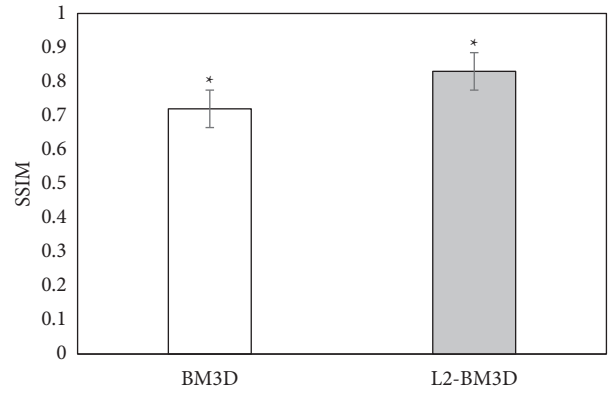

Figure 6: Comparison of SSIM values of different denoising algorithms. Note: "*" indicates that the comparison was statistically significant ($P < 0.05$).

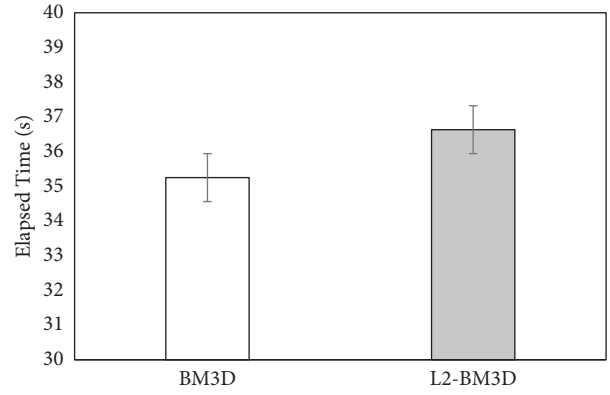

Figure 7: Comparison of running time of different denoising algorithms.

The results showed that peak signal-to-noise ratio (PSNR) and structural similarity index measure (SSIM) of the L_2-BM3D algorithm were better than those of the BM3D algorithm (31.21 dB versus 29.33 dB, 0.83 versus 0.72). However, mean square error (MSE) was less than that of the BM3D algorithm ($P < 0.05$), which showed that the L_2-BM3D algorithm had better denoising effect. The L_2-BM3D algorithm was used by Cao et al. [25] for OCT image processing and it was compared with denosing convolutional neural network (DnCNN) algorithm. The results showed that the L_2-BM3D algorithm had better denoising performance. The epigraph method was used by Gao and Wu [26] to optimize the BM3D denoising algorithm. The results showed that PSNR and SSIM were significantly better

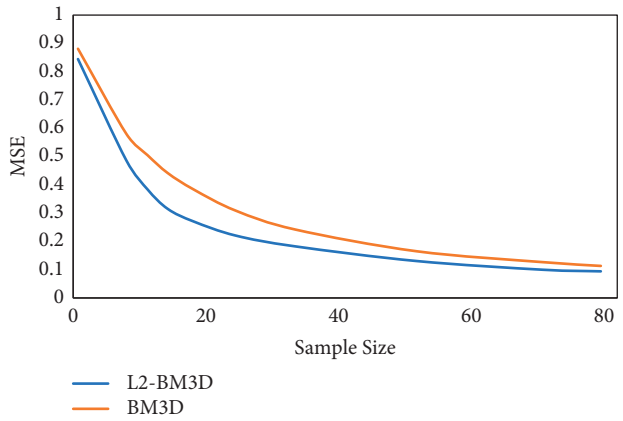

Figure 8: Comparison of the MSE values of different denoising algorithms.

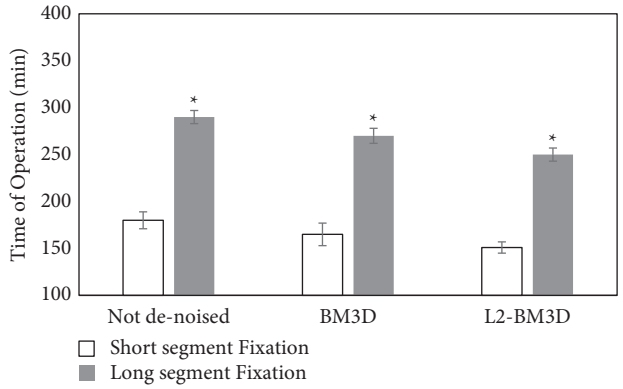

Figure 9: Comparison of the surgical times of different denoising algorithms. Note: "*" indicates that the comparison was statistically significant ($P < 0.05$).

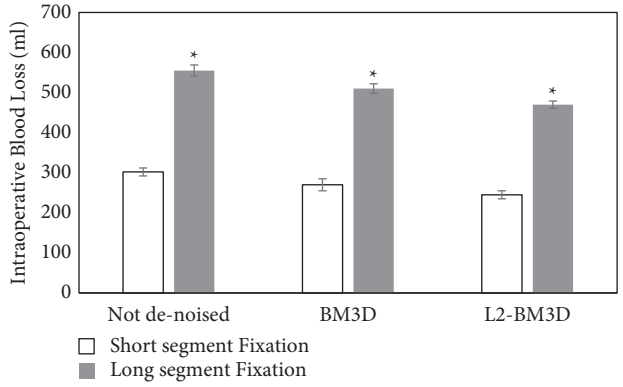

Figure 10: Comparison of the intraoperative blood losses of different denoising algorithms. Note: "*" indicates that the comparison was statistically significant ($P < 0.05$).

than those of other algorithms. The BM3D algorithm could not only be used in the application of MRI images. Lyu et al. [27] also proposed that the regularized improved BM3D algorithm was more effective in CT image denoising.

After that, 120 patients with degenerative lumbar scoliosis in XX Hospital were selected as the research objects. The patients were scanned with MRI, and the denoising effects of different denoising algorithms were compared. The patients were treated with different denoising results. The operation conditions and postoperative follow-up results were compared, and the effects of different denoising algorithms on clinical surgery were analyzed.

Through the assessment of surgical results based on different denoising methods from the surgical time, intraoperative blood loss, and postoperative drainage, it was found that patients with the posterior decompression short-

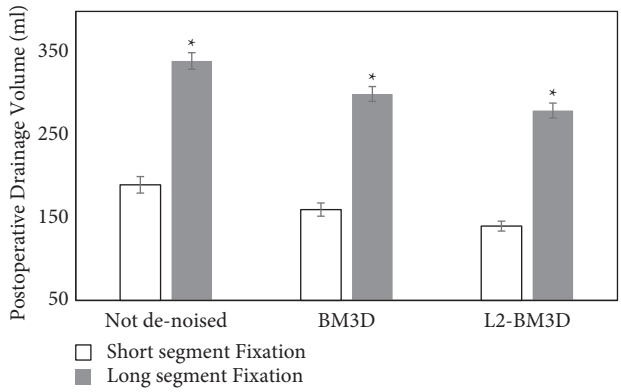

Figure 11: Comparison of the postoperative drainage volumes of different denoising algorithms. Note: "*" indicates that the comparison was statistically significant ($P < 0.05$).

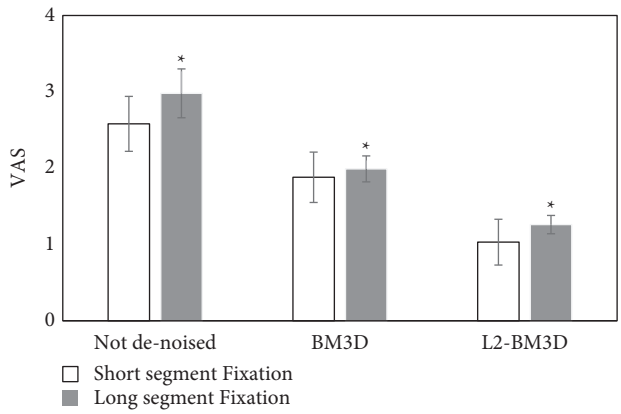

Figure 12: Comparison of VAS scores at the last follow-up after surgery with different denoising algorithms. Note: "*" indicates that the comparison was statistically significant ($P < 0.05$).

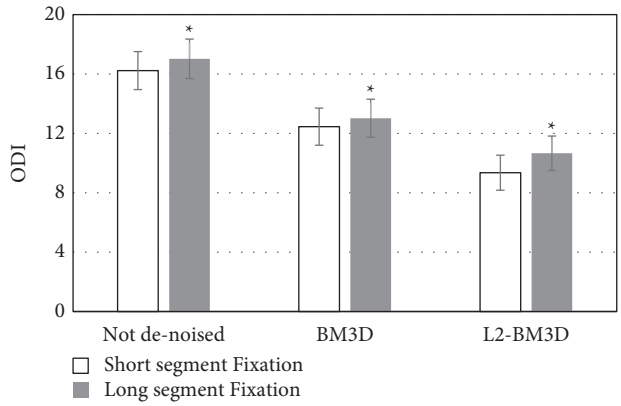

Figure 13: Comparison of ODI at the last follow-up after surgery with different denoising algorithms. Note: "*" indicates that the comparison was statistically significant ($P < 0.05$).

segment fixation based on the L_2-BM3D denoising algorithm had the average surgical time of 151 ± 5.45 min, the average intraoperative blood loss of 255 ± 9.98 mL, and the average postoperative drainage volume of 142 ± 6.27 mL. Besides, the average surgical time, intraoperative blood loss, and postoperative drainage of patients with posterior decompression short-segment fixation based on the L_2-BM3D denoising algorithm were 249 ± 6.41 min, 482 ± 11.31 mL, and 279 ± 10.81 mL, respectively. Thus, the three values of L_2-BM3D denoising algorithm reduced steeply in contrast to those of the BM3D algorithm and the surgical effect without denoising ($P < 0.05$). Finally, the

postoperative follow-up results were evaluated. The results pointed out that the postoperative VAS and ODI of patients with short-segment surgeries based on the L_2-BM3D denoising method were lower, and the difference between the groups was statistically obvious ($P < 0.05$), which suggested that the patient's postoperative recovery effect was better. It was suggested that the L_2-BM3D denoising algorithm could improve the effect of disease diagnosis and treatment of MRI images. It was also conducive to the recovery of patients' diseases, showing a good application prospect of the L_2-BM3D denoising algorithm in medical image processing. The L_2-BM3D denoising algorithm was used by Santos et al. [28] for ultrasonic image denoising research. The BM3D denoising algorithm was used by Chen et al. [29] for the optimization of projection onto convex sets (POCS). The BM3D denoising algorithm was improved by Salehjahromi et al. [30] and CT image was reconstructed by using low rank average algorithm. Good results were achieved in the above research. It showed the application advantages of the BM3D denoising algorithm in imaging.

5. Conclusion

The results of this study revealed that the L_2-BM3D denoising algorithm had a good application prospect in the surgical treatment of degenerative lumbar disease according to the denoising results. Moreover, it can provide information for the denoising processing of MRI medical images, so as to provide a theoretical basis for the surgical treatment of lumbar degeneration. However, the selected patients had only degenerative lumbar scoliosis in this study, and there is no involvement of patients with degenerative lumbar spondylolisthesis and lumbar spinal stenosis. Therefore, the above needs to be further investigated in the future. However, the study shows obviously that the development prospect of intelligent algorithm in the field of medical imaging cannot be underestimated. It has significant effect on improving the diagnosis and treatment of diseases and has high clinical application value.

Data Availability

The data used to support the findings of this study are available from the corresponding author upon request.

Conflicts of Interest

The authors declare no conflicts of interest.

References

[1] M. Teraguchi, R. Yim, and J. P.-Y. Cheung, "The association of high-intensity zones on MRI and low back pain: a systematic review," *Scoliosis and Spinal Disorders*, vol. 13, no. 1, p. 22, 2018.

[2] I. Urits, A. Burshtein, M. Sharma et al., "Low back pain, a comprehensive review: pathophysiology, diagnosis, and treatment," *Current Pain and Headache Reports*, vol. 23, no. 3, p. 23, 2019.

[3] U. Zehra, J. P. Y. Cheung, C. Bow, W. Lu, and D. Samartzis, "Multidimensional vertebral endplate defects are associated with disc degeneration, modic changes, facet joint abnormalities, and pain," *Journal of Orthopaedic Research*, vol. 37, no. 5, pp. 1080–1089, 2019.

[4] Y. Takaishi, M. Okada, D. Fujiwara, A. Uyama, T. Kondoh, and A. Arai, "Surgical results of lumbar degenerative disease with foot drop," *Noshinkeigeka*, vol. 47, no. 8, pp. 851–857, 2019.

[5] S. S. A. Faraj, R. M. Holewijn, M. L. van Hooff, M. de Kleuver, F. Pellisé, and T. M. Haanstra, "De novo degenerative lumbar scoliosis: a systematic review of prognostic factors for curve progression," *European Spine Journal*, vol. 25, no. 8, pp. 2347–2358, 2016.

[6] T. Lan, S.-Y. Hu, Y.-T. Zhang et al., "Comparison between posterior lumbar interbody fusion and transforaminal lumbar interbody fusion for the treatment of lumbar degenerative diseases: a systematic review and meta-analysis," *World Neurosurgery*, vol. 112, pp. 86–93, 2018.

[7] X. L. Zhang, L. Yuan, Y. Zeng, and S. Mai, "Advance in evaluation of lumbar function after long fixation of degenerative scoliosis," *Zhonghua Wai Ke Za Zhi*, vol. 57, no. 5, pp. 397–400, 2019.

[8] F. Vazifehdan, V. G. Karantzoulis, and V. G. Igoumenou, "Sagittal alignment assessment after short-segment lumbar fusion for degenerative disc disease," *International Orthopaedics*, vol. 43, no. 4, pp. 891–898, 2019.

[9] H.-M. Li, R.-J. Zhang, and C.-L. Shen, "Differences in radiographic and clinical outcomes of oblique lateral interbody fusion and lateral lumbar interbody fusion for degenerative lumbar disease: a meta-analysis," *BMC Musculoskeletal Disorders*, vol. 20, no. 1, p. 582, 2019.

[10] E. Wong, F. Altaf, L. J. Oh, and R. J Gray, "Adult degenerative lumbar scoliosis," *Orthopedics*, vol. 40, no. 6, pp. e930–e939, 2017.

[11] J. C. Le Huec, A. Cogniet, S. Mazas, and A. Faundez, "Lumbar scoliosis associated with spinal stenosis in idiopathic and degenerative cases," *European Journal of Orthopaedic Surgery and Traumatology*, vol. 26, no. 7, pp. 705–712, 2016.

[12] W. Kim, J. A. Porrino, K. A. Hood, T. S. Chadaz, A. S. Klauser, and M. S. Taljanovic, "Clinical evaluation, imaging, and management of adolescent idiopathic and adult degenerative scoliosis," *Current Problems in Diagnostic Radiology*, vol. 48, no. 4, pp. 402–414, 2019.

[13] J. T. Bunch, S. D. Glassman, H. R. Underwood et al., "Preoperative full-length standing radiographs and revision rates in lumbar degenerative scoliosis," *Journal of Neurosurgery: Spine*, vol. 28, no. 6, pp. 581–585, 2018.

[14] T. A. Bergen, N. A. Mesropyan, and A. V. Smagina, "Magnetic-resonance imaging under degenerative changes in lumbar spine: state of the art," *Voprosy neirokhirurgii imeni N.N. Burdenko*, vol. 83, no. 4, pp. 104–112, 2019.

[15] H. Kanamoto, Y. Eguchi, Y. Oikawa et al., "Visualization of lumbar nerves using reduced field of view diffusion tensor imaging in healthy volunteers and patients with degenerative lumbar disorders," *British Journal of Radiology*, vol. 90, no. 1080, Article ID 20160929, 2017.

[16] M. Hasan and M. R. El-Sakka, "Improved BM3D image denoising using SSIM-optimized Wiener filter," *EURASIP Journal on Image and Video Processing*, vol. 2018, no. 1, p. 25, 2018 Epub 2018 Apr 17. PMID: 31258615.

[17] T. Zhao, J. Hoffman, M. McNitt-Gray, and D. Ruan, "Ultra-low-dose CT image denoising using modified BM3D scheme

tailored to data statistics," *Medical Physics*, vol. 46, no. 1, pp. 190–198, 2019, Epub 2018 Nov 19. PMID: 30351450.

[18] S. Huang, C. Tang, M. Xu, Y. Qiu, and Z. Lei, "BM3D-based total variation algorithm for speckle removal with structure-preserving in OCT images," *Applied Optics*, vol. 58, no. 23, pp. 6233–6243, 2019, PMID: 31503765.

[19] P. Xu, L. Guo, Y. Feng, and X. Zhang, "[A diffusion-weighted image denoising algorithm using HOSVD combined with Rician noise corrected model]," *Nan Fang Yi Ke Da Xue Xue Bao*, vol. 41, no. 9, pp. 1400–1408, 2021, Chinese.

[20] Y. Chen, W. He, N. Yokoya, and T.-Z. Huang, "Hyperspectral image restoration using weighted group sparsity-regularized low-rank tensor decomposition," *IEEE Transactions on Cybernetics*, vol. 50, no. 8, pp. 3556–3570, 2020, Epub 2019 Sep 2. PMID: 31484156.

[21] M. Beheshti, F. H. Foomany, K. Magtibay et al., "Noise distribution and denoising of current density images," *Journal of Medical Imaging*, vol. 2, no. 2, Article ID 024005, 2015.

[22] J. Jin, E. McKenzie, Z. Fan et al., "Nonlocal means denoising of self-gated and k-space sorted 4-dimensional magnetic resonance imaging using block-matching and 3-dimensional filtering: implications for pancreatic tumor registration and segmentation," *International Journal of Radiation Oncology, Biology, Physics*, vol. 95, no. 3, pp. 1058–1066, 2016.

[23] C. A. N. Santos, D. L. N. Martins, and N. D. A. Mascarenhas, "Ultrasound image despeckling using stochastic distance-based BM3D," *IEEE Transactions on Image Processing*, vol. 26, no. 6, pp. 2632–2643, 2017.

[24] Y. Zhang, J. J. Sun, and J. Sun, "An improved BM3D algorithm based on anisotropic diffusion equation," *Mathematical Biosciences and Engineering*, vol. 17, no. 5, pp. 4970–4989, 2020.

[25] S. Cao, X. Yao, N. Koirala et al., "Super-resolution technology to simultaneously improve optical & digital resolution of optical coherence tomography via deep learning," *2020 42nd Annual International Conference of the IEEE Engineering in Medicine & Biology Society (EMBC)*, vol. 2020, pp. 1879–1882, 2020.

[26] F. Gao and M. Wu, "Deep learning-based denoised MRI images for correlation analysis between lumbar facet joint and lumbar disc herniation in spine surgery," *Journal of healthcare engineering*, vol. 2021, Article ID 9687591, 2021.

[27] Q. Lyu, C. Yang, H. Gao et al., "Technical Note: i," *Medical Physics*, vol. 45, no. 6, pp. 2603–2610, 2018, Epub 2018 Apr 30. PMID: 29663467; PMCID: PMC5997564.

[28] C. A. N. Santos, D. L. N. Martins, and N. D. A. Mascarenhas, "Ultrasound image despeckling using stochastic distance-based BM3D," *IEEE Transactions on Image Processing*, vol. 26, no. 6, pp. 2632–2643, 2017, Epub 2017 Mar 21. PMID: 28333627.

[29] J. Chen, W. Wang, T. Liu, Z. Zhang, and H. Gao, "A POCS super resolution restoration algorithm based on BM3D," *Scientific Reports*, vol. 7, no. 1, p. 15049, 2017.

[30] M. Salehjahromi, Y. Zhang, and H. Yu, "Iterative spectral CT reconstruction based on low rank and average-image-incorporated BM3D," *Physics in Medicine and Biology*, vol. 63, no. 15, p. 155021, 2018.